On the role of block copolymer additives for calcium carbonate crystallization: Small angle neutron scattering investigation by applying contrast variation

Hitoshi Endo[a)]
Max-Planck-Institut für Kolloid- und Grenzflächenforschung, Kolloidchemie, D-14424 Potsdam, Germany and Institut für Festkörperforschung, Forschungszentrum Jülich, D-52425 Jülich, Germany

Dietmar Schwahn
Institut für Festkörperforschung, Forschungszentrum Jülich, D-52425 Jülich, Germany

Helmut Cölfen
Max-Planck-Institut für Kolloid- und Grenzflächenforschung, Kolloidchemie, D-14424 Potsdam, Germany

(Received 8 October 2003; accepted 10 February 2004)

The role of the double-hydrophilic block copolymer poly(ethylen glycol)-*block*-poly(methacrylic acid) (PEG-*b*-PMAA) on the morphogenesis of calcium carbonate ($CaCO_3$) was studied by applying the contrast variation small angle neutron scattering technique. The morphology and size of $CaCO_3$ crystals is strongly affected by the addition of PEG-*b*-PMAA. In order to determine the partial scattering functions of the polymer and $CaCO_3$ mineral, we developed both an experimental and theoretical approach with a sophisticated method of their determination from the scattering intensity. Partial scattering functions give detailed information for each component. In particular, the partial scattering function of the polymer, S_{pp}, shows a monotonic slope with $Q^{-2\text{ to }-3}$ where the scattering vector Q is low ($Q<0.01\,\text{Å}^{-1}$), which is a clear evidence that the polymer within the $CaCO_3$ mineral has a mass fractal dimension. The other partial scattering functions reflected the geometry of the $CaCO_3$ particles or the ''interaction'' of polymer and $CaCO_3$ on a microscopic scale, which leads to a coherent view with S_{pp}. © *2004 American Institute of Physics.*
[DOI: 10.1063/1.1691736]

I. INTRODUCTION

The morphology-controlled synthesis of inorganic materials is a key aspect in the field of materials science, as for ceramics, catalysis, pigments, cosmetics, and so on. It is also well known that biological systems synthesize highly advanced and optimized inorganic materials such as bones, teeth, and shells by controlling their size, shape, structure, and orientation with the help of self-assembled organic molecules like proteins, lipids, etc. These organic additives have been known as quite useful tools to control the nucleation, growth, and alignment of inorganic crystals with complex form,[1] and it is possible to mimic these processes.[2]

Recently, a new class of functional synthetic polymers, the so-called double-hydrophilic block copolymers, was developed for mineralization purposes.[3] These polymers consist of two hydrophilic parts: one block is designed to interact strongly with the inorganic minerals, while the other block does not (or only weakly) interact with mineral surfaces and mainly promotes the solubility in water. In contrast to amphiphilic block copolymers in the hydrophilic–hydrophobic sense, these polymers do not form superstructures in water like micelles, vesicles, and so on, and behave like polyelectrolytes in solution. These polymers have been found to be extraordinarily effective in crystal growth modification or inducing superstructures for several kinds of inorganic materials in water, e.g., barium sulfate,[4,5] calcium phosphate,[6] calcium carbonate,[7,8] barium, cadmium, lead, and mangan carbonate,[9] zinc oxide,[10] lanthanum hydroxide,[11] cadmium tungstate,[12] cadmium sulfide,[13] silver,[14] gold, platinum,[15] and even organic crystals like calcium tartrate[16] or the structure of liquid and solid water were modified.[17] The functions of double hydrophilic polymers have partially been explored in these studies: (i) the chemical composition of the polyelectrolyte block is of great importance for the morphologies,[4] as the same polymer backbone modified with different functional groups gives totally different morphologies; (ii) the molecular weight of the block copolymer, especially that of the functional block, has an influence on the morphologies;[18] (iii) polydispersity seems not to be a dominant control factor, as the results from Refs. 7 and 8 with, respectively, monodisperse and polydisperse polymer fit well into the morphology map from Ref. 8, etc.

In this study we investigate the mineralization of calcium carbonate ($CaCO_3$) crystals in the presence of the double-hydrophilic block copolymer poly(ethylen glycol)-*block*-poly(methacrylic acid) (PEG-*b*-PMAA). These $CaCO_3$ crystals were synthesized by crystallization at room temperature in water and in the presence of PEG-*b*-PMAA. It has been found that the morphology is mainly affected by the ratio [polymer]/[$CaCO_3$] and the *p*H of the solution.[8] Moreover, in Ref. 8, a morphogenesis of shapes from rod-to-dumbbell-to-sphere is indicated very similar to observations

[a)]Author to whom all correspondence should be addressed. Electronic mail: h.endo@fz-juelich.de

for fluorapatite in gelatin gels.[19,20] However, the formation mechanisms behind these inorganic structures remain unknown. It is furthermore believed that investigations of these morphogenesis scenarios will provide not only insight into polymer driven formation of complex mineral shapes but also will allow further insight into the mechanisms of biomineralization.

We investigated the structure of PEG-*b*-PMAA for the formation of $CaCO_3$ particle superstructures by using the contrast variation *small angle neutron scattering* (SANS) technique. A unique possibility of neutron scattering is isotope labeling with deuterium, i.e., the scattering lengths of atoms for neutrons depend on the spin status of the nuclei of the scatterer, so that the coherent scattering length of the hydrogen is negative (-3.74 fm), on the other hand, that of deuterium is positive (6.67 fm). Therefore with neutrons as a probe, contrast variation techniques based on the hydrogen/deuterium replacement can be used to modify the visibility of different components in the system.[21]

The SANS contrast variation method has been widely used for structural investigations of complex systems, e.g., colloidal spheres,[22,23] polymer aggregates or micelles,[24,25] microemulsions,[26,27] biological macromolecules,[28,29] etc. However, difficulties of this method are that it is highly model dependent[23,25,27] and needs accurate determination of the scattering length densities of each component.[22,24] Therefore these problems have to be solved in order to apply this method successfully. Recently, Endo *et al.* demonstrated a sophisticated contrast variation technique to evaluate the structure of polymers in ternary microemulsions (water, oil, and nonionic surfactant) with 15 different contrasts on the two-dimensional contrast plane, i.e., the contrasts of oil and surfactant were varied by mixing the protonated and deuterated chemicals.[26,30] The significance of this achievement was that even though the polymer concentration was very low ($\sim$0.5 vol %), the intensities could be decomposed into the partial scattering functions on the basis of a precise knowledge of all scattering contrasts.

We tried to make the best use of this technique for the determination of the structure of polymers within the $CaCO_3$ particles.[31] Since the scattering signal from the polymer is very weak in our system, very precise contrast variation experiments were needed. We also needed further theoretical development for the quantitative decomposition of the achieved intensities into partial scattering functions. We found that the scattering intensity of the ternary system can be described by their partial scattering functions of the three single species (squared terms) assuming incompressibility. The obtained polymer scattering as well as the polymer–$CaCO_3$ cross term clearly show the geometry of the polymer in the hybrid particles.

II. SCATTERING THEORY

A. Partial scattering functions on the basis of incompressibility

Assuming a multicomponent system with p different species, the scattering intensity $(d\Sigma/d\Omega)(Q)$ can be split into partial scattering functions, S_{ij}, according to Refs. 21 and 32 as follows:

$$\frac{d\Sigma}{d\Omega}(Q)=\sum_{i=1}^{p}\rho_i^2 S_{ii}(Q)+2\sum_{i<j}^{p}\rho_i\rho_j S_{ij}(Q), \tag{1}$$

where Q is the scattering wave number defined by $Q=(4\pi/\lambda)\sin(\Theta/2)$ with the scattering angle Θ and the neutron wavelength λ. A partial scattering function S_{ij} is defined by

$$S_{ij}(Q)=\frac{1}{V}\int\int\langle\delta c_i(\vec{r})\,\delta c_j(\vec{r}\,')\rangle \times\exp\{i\vec{Q}\cdot(\vec{r}-\vec{r}\,')\}d^3\vec{r}\,d^3\vec{r}\,', \tag{2}$$

where V is the scattering volume and $\delta c_i(\vec{r})$ is the fluctuation part of the volume fraction of component i, $c_i(\vec{r})$, at position $\vec{r}$ according to

$$\delta c_i(\vec{r})=c_i(\vec{r})-\overline{c_i} \tag{3}$$

with the average concentration, $\overline{c_i}$, that is $\overline{c_i}=\int_V c_i(\vec{r})d^3\vec{r}/V$. The relationship

$$\sum_{i=1}^{p}\delta c_i(\vec{r})=0 \tag{4}$$

is obtained assuming incompressibility. ρ_i is the scattering length density,

$$\rho_i=\frac{\Sigma_z b_z}{v_i}, \tag{5}$$

where b_z is the coherent scattering length of the individual atom z in the molecule i, and v_i is the volume of the corresponding molecule. The partial scattering function as defined in Eq. (2) contains information of intra- and intercorrelations of the species, i.e., involves a form factor and a structure factor.

We will now present a further derivation of the scattering function of Eq. (1), which leads to a very concise expression. At the beginning, multiplying Eq. (4) by $\delta c_k(\vec{r}\,')\exp\{-iQ(\vec{r}-\vec{r}\,')\}$ and doing the integratation $\int_V d^3\vec{r}$, we obtain

$$\sum_{i=1}^{p}S_{ki}(Q)=0. \tag{6}$$

In Eq. (6), the index k indicates each species, i.e., $1\leqslant k\leqslant p$, therefore p relationships about partial scattering functions are obtained, which means that the relation of Eq. (6) allows one to eliminate one species from Eq. (1).

Furthermore, the relationship given by Eq. (6) leads to the form as

$$\begin{aligned}S_{kk}(Q)&=-\sum_{i\neq k}^{p}S_{ki}(Q)\\&=-\sum_{i\neq k}^{p}\left\{\sum_{j\neq k}^{p}S_{ij}(Q)\right\}\\&=\sum_{i\neq k}^{p}S_{ii}(Q)+2\sum_{i,j\neq k;i<j}^{p}S_{ij}(Q).\end{aligned} \tag{7}$$

Equation (7) is equivalent to the Babinet principle described in Appendix A [see Eq. (A6)]. It is mentioned that Eq. (7)

does not contain any scattering lengths, i.e., Eq. (7) simply gives a general relationship of partial scattering functions on the basis of incompressibility.

In the case of ternary systems, there are totally six partial scattering functions and three partial scattering functions are at least necessary for the description of the intensity based on the incompressibility hypothesis. Let us assume a ternary system with species 1, 2, and 3. According to Eq. (7), we can find the relationships as follows:

$$\begin{aligned} 2S_{12}(Q) &= -S_{11}(Q) - S_{22}(Q) + S_{33}(Q), \\ 2S_{23}(Q) &= S_{11}(Q) - S_{22}(Q) - S_{33}(Q), \\ 2S_{13}(Q) &= -S_{11}(Q) + S_{22}(Q) - S_{33}(Q). \end{aligned} \tag{8}$$

This means that all the cross terms can be substituted by the squared terms, so that the scattering intensity can be described only by the partial scattering functions S_{ii} where $1 \leqslant i \leqslant 3$, i.e., we have

$$\begin{aligned} \frac{d\Sigma}{d\Omega}(Q) = &(\rho_1-\rho_2)(\rho_1-\rho_3)S_{11}(Q) + (\rho_2-\rho_1)(\rho_2-\rho_3) \\ &\times S_{22}(Q) + (\rho_3-\rho_1)(\rho_3-\rho_2)S_{33}(Q). \end{aligned} \tag{9}$$

Equation (9) is useful for the contrast variation technique of neutron scattering, since the values of the decomposed partial scattering functions S_{ii} must always be positive, and these S_{ii} are much easier to interpret compared with the cross terms. This equation has been derived also by Pyckhout *et al.* independently.[33]

B. Decomposition of scattering intensities into partial scattering functions by contrast variation

When a neutron scattering experiment is performed on the same samples with *m* different contrasts by using isotope mixtures, the obtained coherent intensities yield a set of linear equations which is expressed as

$$\vec{I} = \underline{M} \cdot \vec{s}, \tag{10}$$

where $\vec{I}$ represents a vector of intensities, i.e.,

$$\vec{I} = \begin{pmatrix} \left.\frac{d\Sigma}{d\Omega}\right|_1(Q) \\ \vdots \\ \left.\frac{d\Sigma}{d\Omega}\right|_m(Q) \end{pmatrix}, \tag{11}$$

$\underline{M}$ is a matrix consisting of scattering length densities, and $\vec{s}$ consists of the partial scattering functions. For a ternary system with components 1, 2, and 3, $\underline{M}$ and $\vec{s}$ are given based on Eq. (9) as

$$\underline{M} = \begin{pmatrix} {}^1\Delta_{12}{}^1\Delta_{13} & {}^1\Delta_{21}{}^1\Delta_{23} & {}^1\Delta_{31}{}^1\Delta_{32} \\ \vdots & & \\ {}^m\Delta_{12}{}^m\Delta_{13} & {}^m\Delta_{21}{}^m\Delta_{23} & {}^m\Delta_{31}{}^m\Delta_{32} \end{pmatrix} \tag{12}$$

and

$$\vec{s} = \begin{pmatrix} S_{11}(Q) \\ S_{22}(Q) \\ S_{33}(Q) \end{pmatrix}, \tag{13}$$

where ${}^m\Delta_{ij} = \rho_i - \rho_j$ for the *m*th measurement.

In order to obtain the unknown partial scattering functions, S_{ij}, evaluation of the orthogonal matrix $\underline{M}^T$ is necessary. Since all the scattering length densities can be calculated by knowing the chemical structure and mass density of the components, $\underline{M}^T$ can be determined with high accuracy. In the case of *p* component systems, there are ${}_pC_2 = p!/\{(p-2)! \cdot 2!\}$ unknown partial scattering functions (see Appendix A), so that at least ${}_pC_2$ measurements with different contrasts are necessary. If the number of measurements is the same as that of the unknown partial scattering functions, it is possible to find a unique solution of $\vec{s}$. Otherwise the set of equations is overdetermined (called *degenerate*), which can be solved by a "*singular value decomposition*" algorithm for each *Q* value. This algorithm is equivalent to a least squares fit.[34]

It has to be mentioned that Eq. (10) is not unique, e.g., Eqs. (12) and (13) can be replaced on the basis of Eq. (A7) as follows:

$$\underline{M} = \begin{pmatrix} {}^1\Delta_{13}^2 & 2{}^1\Delta_{13}{}^1\Delta_{23} & {}^1\Delta_{23}^2 \\ \vdots & & \\ {}^m\Delta_{13}^2 & 2{}^m\Delta_{13}{}^m\Delta_{23} & {}^m\Delta_{23}^2 \end{pmatrix} \tag{14}$$

and

$$\vec{s} = \begin{pmatrix} S_{11}(Q) \\ S_{12}(Q) \\ S_{22}(Q) \end{pmatrix}, \tag{15}$$

where "*component 3*" is eliminated. But in this case, S_{12} will be determined, which is not so easy to interpret.

III. EXPERIMENTAL SECTION

A. Samples

We prepared calcium carbonate ($CaCO_3$) crystals based on the knowledge given in Ref. 8. A block copolymer poly(ethylene glycol)-*block*-poly(methacrylic acid) (PEG-*b*-PMAA, PEG=3000 g/mol, PMAA=700 g/mol) was obtained from Th. Goldschmidt AG, Essen (Germany), where the PMAA-block interacts strongly with $CaCO_3$ while the PEG-block mainly promotes the solubilization in water. The polymer was purified by exhaustive dialysis and used in the crystallization of $CaCO_3$. All other chemicals were purchased from Aldrich and used without further purification.

The synthesis of $CaCO_3$ was carried out by means of precipitation, i.e., aqueous solutions of Na_2CO_3 and PEG-*b*-PMAA were first prepared and adjusted to a desired *p*H (e.g., *p*H=8.5) by using HCl or NaOH, then a solution of $CaCl_2$ was mixed quickly with the *p*H-adjusted solution under vigorous stirring at room temperature. A detailed description can be found also in Ref. 8.

The ion concentrations both of $CaCl_2$ and Na_2CO_3 were 0.4 *normal*, where the concentrations were much higher than in the case of Ref. 8. We prepared the crystals with a mass ratio $[\text{polymer}]/[CaCO_3] = 0.3$ and 0.9 with *p*H=8.5. After the reactions, the crystals were separated from the polymer solution by sedimentation and rinsed three times with pure water, so that the polymer which did not react with $CaCO_3$ was removed almost completely.

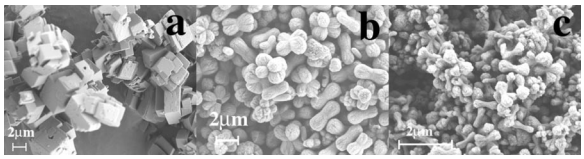

FIG. 1. SEM images for $CaCO_3$ particles with different morphologies: (a) without polymer, (b) with polymer ([polymer]/[$CaCO_3$]=0.3), and (c) with polymer ([polymer]/[$CaCO_3$]=0.9). Each $CaCO_3$ particle was prepared in the solution with pH≈8.5 at the beginning (see the text).

The obtained crystals were characterized by scanning electron microscopy, thermogravimetry analysis, and wide angle x-ray scattering (WAXS) measurements to confirm the morphologies, fractions of the polymer in $CaCO_3$ and crystal structures, respectively. In Fig. 1, the observed scanning electron microscopy pictures of the materials are shown. We obtained mainly dumbbell morphologies for both concentrations [polymer]/[$CaCO_3$]=0.3 and 0.9, and could observe that the sizes of the crystals were strongly affected by the initial polymer concentration in the solutions. The detailed results about the characterizations are given in Appendix C.

B. Small angle neutron scattering

SANS experiments were performed at the KWS-1 SANS diffractometer at the FRJ-2 reactor of the Forschungszentrum Jülich. The details of the instrumental setting can be found in Ref. 35. We used a neutron wavelength of $\lambda=7$ Å with a $\Delta\lambda/\lambda=20\%$ full width at half maximum. The covered scattering wave number Q was $0.002\,\text{Å}^{-1}<Q<0.2\,\text{Å}^{-1}$ in reciprocal space.

The calcium carbonate ($CaCO_3$) crystals were mixed with a D_2O and H_2O mixture for performing the contrast variation experiments. To avoid sedimentation, a special type of cell was prepared which has both an input and an output nozzle at the top and bottom. A silicon tube was connected between the cell and a peristaltic pump, which circulated the solution during the experiments.

The data sets were normalized to absolute intensity by the incoherent scattering of a Lupolen secondary standard.

Scattering length densities of the polymer and $CaCO_3$ were calculated on the basis of their chemical structures and mass densities. The mass density for the block-co-polymer was calculated from 1.10 [g/cm^3] for the PMAA-block[36] and 1.125 [g/cm^3] for the PEG-block.[25] Since both the PMAA-block and the PEG-block are protonated, the scattering contrast between these blocks is rather weak. Therefore the scattering length density of the block copolymer approximated the average value of these two blocks. A mass density 2.71 [g/cm^3] is used for the calcite $CaCO_3$ mineral.[37] The resulting scattering length densities are listed in Table I.

TABLE I. Calculated scattering length densities for the components: ρ_p for the polymer, ρ_c for $CaCO_3$, and ρ_w for the water mixtures used for the contrast variation. The given "error" is the averaged difference (percentage) between an experimental value and a reconstructed value.

[Polymer]/[$CaCO_3$] increment	0.3 ρ_w (10^{10} cm^{-2})	0.9 ρ_w (10^{10} cm^{-2})
1	4.896	4.896
2	4.784	4.811
3	4.727	4.730
4	4.643	4.642
5	4.489	4.476
D_2O	6.355	6.355
Error	2.364%	2.212%
	ρ_p [10^{10} cm^{-2}]	ρ_c [10^{10} cm^{-2}]
	0.783	4.689

IV. RESULTS AND DISCUSSIONS

The present system is a ternary one with the components $CaCO_3$, polymer, and water. Therefore, when the contrast between $CaCO_3$ and water is completely matched, the scattering signal should come only from the polymer.

Figure 2 shows the scattering results obtained from the $CaCO_3$/polymer hybrid crystals, where the intensities were obtained with different scattering contrasts and normalized by the volume fractions of $CaCO_3$. At low Q, the intensity with D_2O solvent, where the scattering signal comes from both the polymer and $CaCO_3$, is roughly two orders of magnitude higher than the intensity with the contrast matched water. Here the mixture of D_2O and H_2O was prepared to match the scattering length density of $CaCO_3$ so that the scattering should arise only from the polymer in the system. It is a significant difficulty to extract the polymer scattering from such a measurement, as a small mismatch of the scattering contrast between $CaCO_3$ and water can seriously disturb the scattering from the polymer because of the vast difference between the scattering contribution from $CaCO_3$ and the polymer. This may happen in the low-Q range. On the other hand, this contrast matching experiment confirms that the low-Q signal with D_2O solvent is mainly dominated by $CaCO_3$. Therefore, we can conclude that the volume fraction of the polymer in $CaCO_3$ is quite minute, since a scattering intensity is proportional to the volume fraction of the scatterer. This result is consistent with the results obtained by thermogravity measurements presented in Appendix C 2.

To solve the "mismatch" problem, we performed contrast variation experiments. As a starting point, a D_2O/H_2O

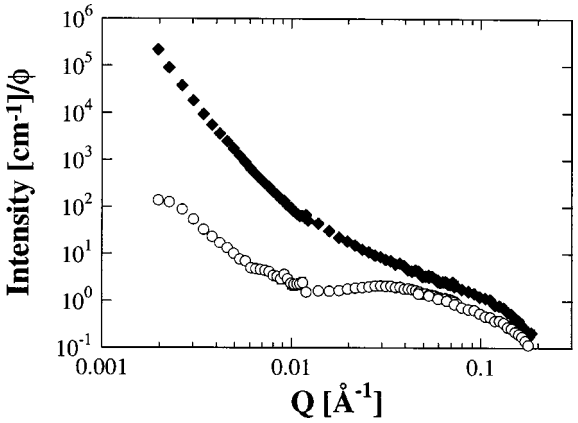

FIG. 2. Normalized scattering intensities obtained from dumbbell morphology ([polymer]/[$CaCO_3$]=0.3): (○) with matching water (only polymer is visible), and (◆) with D_2O (both polymer and $CaCO_3$ are visible).

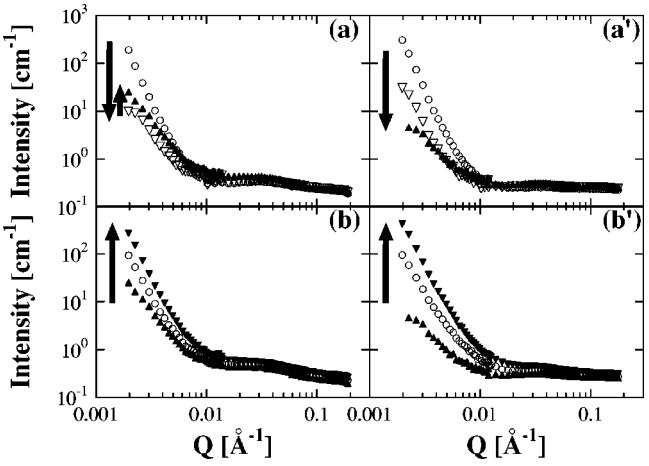

FIG. 3. Scattering intensities obtained for the contrast variation series. Left curves [(a) and (b)] are from $CaCO_3$ prepared with polymer concentration [polymer]/[$CaCO_3$]=0.3, and right curves [(a′) and (b′)] are from [polymer]/[$CaCO_3$]=0.9. The arrangement of the curves is as follows: in (a) and (a′) increment 1(○), 2(▽), and 3(▲); in (b) and (b′) increment 3(▲), 4(○), and 5(▽), which corresponds to the numbers in Table I.

mixture was prepared to match the scattering length density of $4.9\times10^{10}\,\mathrm{cm}^2$, which is slightly larger than that of $CaCO_3$ ($4.69\times10^{10}\,\mathrm{cm}^2$). A stepwise reduction of the scattering length density of water was achieved by adding minute amounts of H_2O (between 20 and 60 mg). The addition of H_2O was done with a microsyringe and the mass of added H_2O was checked with a chemical balance. In Table I the estimated scattering length densities of the polymer, $CaCO_3$, and the mixtures with H_2O and D_2O for each step are shown. The quality of these scattering length densities was checked with the method described in Appendix B.

In Fig. 3 the obtained scattering profiles for the contrast variation experiments are exhibited. It is clearly shown that the intensity at low-Q once decreases with the addition of H_2O, and increases after the scattering contrast of the aqueous solution crosses the contrast of $CaCO_3$. These data sets were used to achieve the partial scattering functions on the basis of Eqs. (12) and (13) with knowing all the scattering contrasts of the components. Additionally, we added the results measured with the D_2O solvent, which improved the stability of the numerical solution. The ternary system contains three unknowns, i.e., S_{cc}, S_{pp}, and S_{ww}, where the subscripts c, p, and w represent the components $CaCO_3$, polymer, and water respectively, according to Eq. (9); therefore the full use of the experimental data set leads to an overdetermined set of six equations (five contrast variations plus D_2O solvent). These equations were solved by the method of singular-value decomposition, as described in Sec. II B. Figure 4 displays the resulting partial scattering functions S_{cc}, S_{pp}, and S_{ww}.

The scattering intensities were reconstructed on the basis of the obtained partial scattering functions, i.e., the backsubstitution of the partial scattering functions into Eq. (10) leads to the corresponding scattering intensity. The reconstructed intensities are compared with the experimental results in Fig. 5. A nearly perfect reconstruction is achieved. This result confirms that the model in the basis of Eq. (9) for a description of the scattering intensities with three partial scattering functions and the calculated scattering length densities are appropriate.

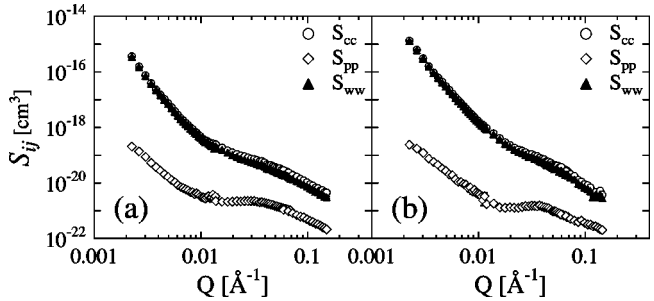

FIG. 4. Decomposed partial scattering functions: S_{cc}(○), S_{pp}(◇), and S_{ww}(▲), respectively, for (a) sample [polymer]/[$CaCO_3$]=0.3 and (b) sample [polymer]/[$CaCO_3$]=0.9.

A. Squared terms

In Fig. 4 all the squared terms S_{cc}, S_{pp}, and S_{ww} of sample [polymer]/[$CaCO_3$]=0.3 (a) and sample [polymer]/[$CaCO_3$]=0.9 (b) are exhibited. These results are quite reasonable. First of all, all partial scattering functions are positive. That is a demand of the squared terms of partial scattering functions, S_{ii}. Second, $S_{cc}\approx S_{ww}$ is fulfilled for the whole Q range. This is expected from the Babinet principle based on a geometrical discussion when the polymer concentration in the $CaCO_3$ crystals is very small [see Eq. (A3)], therefore the system can be regarded as pseudo-binary one.

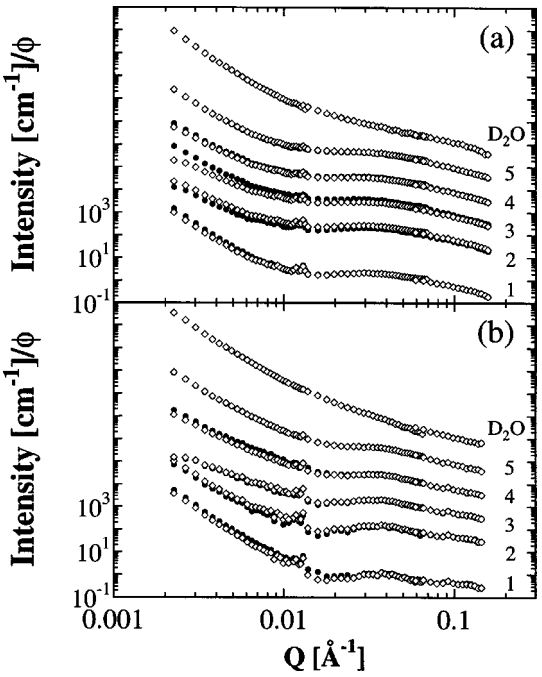

FIG. 5. Comparison between the obtained scattering intensities (●) and the reconstructed intensities (◇) for (a) sample [polymer]/[$CaCO_3$]=0.3 and (b) sample [polymer]/[$CaCO_3$]=0.9. The curves are separated from each other by a shift factor of 10 or 100. The numbers beside the curves indicate the corresponding increments exhibited in Table I.

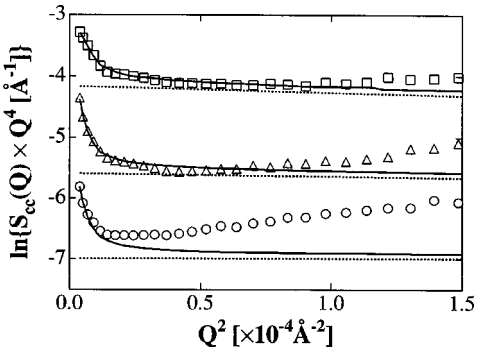

FIG. 6. Porod plot for S_{cc} with the initial condition [polymer]/[$CaCO_3$] = 0 (○), 0.3 (△), and 0.9 (□). The solid lines are the fitting with Eq. (17) considering the resolution effect, while the dashed lines are calculated using the same parameters as the solid lines without the resolution effect. The resolution effect is evident. It is also clearly visible that the polymer addition leads to increase the surface-to-volume ratio S/V.

We will discuss the behavior of S_{cc} and S_{pp} in further detail in the following.

The partial scattering function of $CaCO_3$, S_{cc}, consists of two parts: at low-Q, an approximate Q^{-4} slope is clearly shown, which corresponds to the interface scattering (the Porod law)[38] described by

$$\frac{d\Sigma}{d\Omega}(Q) = 2\pi(\rho_c - \rho_w)^2 \frac{S}{V} Q^{-4} \exp(-\sigma^2 Q^2), \tag{16}$$

where S/V is the specific amount of surface (an interface area per unit volume) and σ is the Gaussian roughness of the interface.[39] Figure 6 presents Porod plots according to $\ln[(d\Sigma/d\Omega)(Q)Q^4]$ vs Q^2 for S_{cc}. At low Q in Fig. 6, the intensities increase and deviate from Q^{-4}, which is normally understood as an effect of curvatures of the interface and known as the Kirste–Porod law.[40,41] However, in our case because of a Q^{-4} behavior at low Q limit, the forward scattering intensities are very strong, so that we cannot ignore the resolution effects of our diffractometer. Resolution effects were taken into account by convolution of a model function and a Gaussian type resolution function.[42] Since Eq. (16) gives an unrealistically large value near $Q=0$, the convolution process is easily destroyed. We made use of Beaucage's approach, where the form factor is described by the Guinier regime at low Q and the scale-limited Porod regime at high Q.[43] For a single object with a sharp interface and a radius of gyration, R_g, the form factor is given as

$$\frac{d\Sigma}{d\Omega}(Q) = \Delta\rho^2 \left\{ \phi V \exp\left(\frac{-Q^2 R_g^2}{3}\right) + 2\pi \frac{S}{V} \left[\frac{\{\mathrm{erf}(QR_g/\sqrt{6})\}^3}{Q} \right]^4 \right\}, \tag{17}$$

in which ϕ is the volume fraction of the object in the system and V is the volume of the object, which can be calculated as

$$V = \int_0^\infty 4\pi r^2 \gamma_G(r) dr = \frac{8\pi}{3} \sqrt{\frac{\pi}{3}} R_g^3, \tag{18}$$

with the correlation function for the Guinier regime, $\gamma_G(r) = \exp(-3r^2/4R_g^2)$.[43] Equation (17) is constant at low Q and shows Q^{-4} behavior at high Q, so that this equation also allows a convolution procedure at low Q, and moreover, it has only the fitting parameters R_g (Ref. 44) and S/V, while the others must be known. In Fig. 6 the lines correspond to the fits with Eq. (17) taking the resolution effect into account, on the other hand, the dashed lines were calculated without the convolution by using the same parameters for comparison. The effect of resolution can be easily seen at low Q. For the sake of better fits with Eq. (17) in Fig. 6, the second term was multiplied by $\exp(-\sigma^2 Q^2)$ as in the case of Eq. (16), since Eq. (17) approximates to $2\pi\Delta\rho^2(S/V)Q^{-4}$ at high Q. The resulting parameters are listed in Table II. The radii of gyration R_g from scattering results can be compared with the observed SEM images using a model calculation for the radii of gyration for dumbbell and rhombohedral forms. The numeric details of this calculation are given in Appendix D. For a calcite rhombohedral crystal the interior angle $\alpha = 46°$ is given,[37] therefore the corresponding length of the side $L = 1.1\,\mu$m. For dumbbell forms, $R_g = 0.99\,\mu$m for the samples prepared with [polymer]/[$CaCO_3$] = 0.3 and 0.38 μm for [polymer]/[$CaCO_3$] = 0.9 were calculated, respectively, for several representative particles chosen from the SEM pictures. R_g are nevertheless in the same order of magnitude with the particles observed by the SEM pictures, though the distribution of the size or the topology of particles was not taken into account for the sake of simplification as size distribution and topology affect its radius of gyration significantly. We emphasize here that the resolution effects are crucial in this case.

TABLE II. Fitting results obtained from the low Q part of S_{cc} with Eq. (17). The radius of gyration, R_g, the specific amounts of surface, $(S/V)/\phi$, and the roughness of surface of $CaCO_3$, σ. $R_g^\dagger$ is estimated from SEM pictures (Fig. 1).

Sample [polymer]/[$CaCO_3$]	R_g (μm)	$(S/V)/\phi_{CaCO_3}$ (Å^{-1})	σ (Å)	$R_g^\dagger$ (μm)
0	0.77±0.00	(1.46±0.00)×10^{-4}	0±9	⋯
0.3	1.28±0.00	(5.94±0.00)×10^{-4}	22±2	0.99
0.9	0.62±0.02	(2.47±0.00)×10^{-3}	32±1	0.38

The difference of the specific amount of surface normalized by the volume fraction $(S/V)/\phi_{CaCO_3}$ for each sample is quite obvious. It is apparent that the polymer induces a more complex shaped surface of $CaCO_3$, since S/V can be related to the topology of interfacial structures. The interface roughness, σ, tends to increase also with the addition of polymer.

At high Q an additional scattering is observed, which was also fitted by Eq. (17). In Fig. 7 the partial scattering functions for three different samples with the results of fitting are displayed, and the resulting parameters are given in Table III. The influence of the polymer addition is apparent. It is clear that the achieved radii of gyration, r_g,[45] and the specific amount of surface, S/V, are affected by the polymer addition, where r_g is almost constant for the [polymer]/[$CaCO_3$] ratios of 0.3 and 0.9. As shown in Fig. 4, $S_{cc} \approx S_{ww}$ holds for all given Q; however, S_{cc} is almost the same (slightly larger) as S_{ww} at high Q, where r_g is determined. Therefore, the origin of r_g should be mainly the small

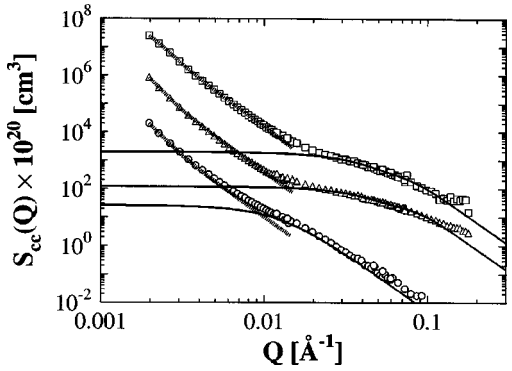

FIG. 7. Partial scattering functions S_{cc} with the initial condition [polymer]/[$CaCO_3$]=0 (○), 0.3 (△), and 0.9 (□). The intensity scale applies directly to the lowest curve, and the others are successively shifted by a factor of 10. Solid lines correspond to fits with Eq. (17) for high Q. Dashed lines are also fits with Eq. (17) for low Q which are identical to the fits in Fig. 6.

structure between the water and $CaCO_3$ crystals, which may be related to σ in Eq. (16). These results tell that the addition of polymer also changes the interface structure of $CaCO_3$ dramatically. We guess that this surface roughness is a trace from the aggregation of small $CaCO_3$ particles which may be formed during the early stages of the reaction.

The extracted partial scattering function of the polymer S_{pp} contains information about the arrangement and conformation of the used double-hydorophilic block copolymer PEG-*b*-PMAA in the $CaCO_3$ crystals. S_{pp} may be composed of two parts, namely, on one hand single polymer chain scattering is observed at high Q; on the other hand, the intensity increases monotonically at low Q. This monotonic slope at low Q shows $I(Q) \propto Q^{-3}$, which is clear evidence of a nearly homogeneous distribution of the polymer in $CaCO_3$. Moreover, we assume that this slope proportional to $Q^{-2 \text{ to } -3}$ originates from a mass fractal structure. To evaluate this scattering profile, we applied the function as follows:[46,47]

$$S_{pp}(Q) \propto \left[\frac{1}{(1+Q^2\xi^2)^{(D_f-1)/2}} \times \frac{\sin\{(D_f-1)\arctan(Q\xi)\}}{(D_f-1)Q\xi} \right], \tag{19}$$

where $\Gamma(x)$ is the gamma function, D_f is the mass fractal dimension, and ξ is the length of the upper cutoff.[46,47] The corresponding pair-correlation function $G(r)$ is given by

$$G(r) \propto (1/r^{D-D_f}) \exp(-r/\xi), \tag{20}$$

TABLE III. Fitting results obtained from the high Q part of S_{cc} with Eq. (17). The amplitude factor for the high Q part, ϕ, the radius of gyration r_g, and the specific amounts of surface, S/V.

Sample [polymer]/[$CaCO_3$]	ϕ	r_g (Å)	S/V (Å^{-1})
0	$(8.3\pm1.0)\times10^{-7}$	153±31	$(8.1\pm0.5)\times10^{-4}$
0.3	$(2.1\pm0.1)\times10^{-5}$	40±2	$(1.9\pm0.1)\times10^{-1}$
0.9	$(2.9\pm0.7)\times10^{-5}$	44±7	$(1.7\pm0.4)\times10^{-1}$

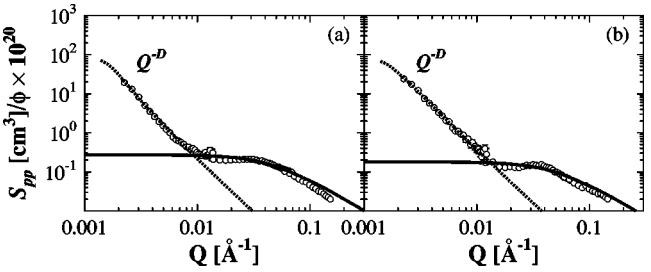

FIG. 8. Partial scattering functions for polymer S_{pp}; (a) sample [polymer]/[$CaCO_3$]=0.3 and (b) sample [polymer]/[$CaCO_3$]=0.9. Lines correspond to fits with Eqs. (19) and (21), see the text.

with the space dimension D, and $D_f < D = 3$ in our case. At small r in Eq. (20), the polymer centers cannot approach closer than a radius $2R_p$ of the other polymers, so that $G(r)=0$ for $r<2R_p$. In this situation, Eq. (19) decreases quickly and the scattering intensity is dominated by the polymer-coil scattering, which is described as

$$S_{\text{coil}}(Q) \propto \left\{ \exp\left(\frac{-Q^2\mathcal{R}_g^2}{3} \right) + B\left[\frac{\{\text{erf}(wQ\mathcal{R}_g/\sqrt{6})\}^3}{Q} \right]^P \right\}, \tag{21}$$

with Q^{-P} asymptote with the Flory exponent $P=5/3$, and the radius of gyration of polymer $\mathcal{R}_g$, and $w=1.06$.[48] B is a prefactor and defined by

$$B = (P/\mathcal{R}_g^P)\Gamma(P/2). \tag{22}$$

Equation (21) is close to the Debye equation for an ideal (Gaussian) chain. Therefore we fitted the data with Eq. (19) at low-Q ($Q<0.01$ Å) and with Eq. (21) at high-Q ($Q>0.02$ Å).

In Fig. 8 the obtained partial scattering functon S_{pp} and the corresponding fitted curve with Eqs. (19) and (21) are shown.

In the middle Q range between these two regimes, a plateau region is observed for both S_{pp} of sample [polymer]/[$CaCO_3$]=0.3 and 0.9. This plateau region is clear evidence that the polymers are isolated as individual chains. If the polymer would have formed a network-like structure, such a plateau region cannot appear and a continuous decrease of the scattering intensity should be observed.[47]

The obtained main parameters are $\mathcal{R}_g=35$ Å and $D_f=2.7$ for the sample prepared with the initial condition [polymer]/[$CaCO_3$]=0.3, and $\mathcal{R}_g=32$ Å and $D_f=2.6$ are achieved for [polymer]/[$CaCO_3$]=0.9 (see Table IV). The obtained $\mathcal{R}_g$ are quite reasonable for its molecular weight.[49] The upper cutoff length ξ can be related to the radius of gyration $\mathbb{R}_g$ by[50]

$$\mathbb{R}_g^2 = \tfrac{1}{2}(D_f-1)D_f(D_f+1)\xi^2, \tag{23}$$

so that the calculated $\mathbb{R}_g$ from the obtained D_f and ξ are 0.8 μm for [polymer]/[$CaCO_3$]=0.3 and 0.3 μm for [polymer]/[$CaCO_3$]=0.9. These values are comparable with R_g obtained from S_{cc} (see Table III), therefore ξ may originate in the size of a $CaCO_3$ particle.

We suggest that the fractal dimension $D_f \approx 2.6$–2.7 means a distribution of the individual polymers (i.e., the cen-

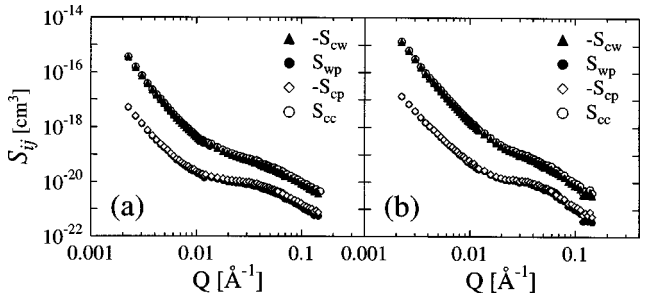

FIG. 9. Cross terms of $CaCO_3$–water, $-S_{cw}$(▲); water–polymer, S_{wp}(●); and $CaCO_3$–polymer $-S_{cp}$(◇), respectively, for (a) sample [polymer]/[$CaCO_3$]=0.3 and (b) sample [polymer]/[$CaCO_3$]=0.9. It is mentioned that S_{cw} and S_{cp} are negative in the measured Q range, so that $-S_{ij}$ are displayed for the double logarithmic scale. The squared term of $CaCO_3$, S_{cc}(○), is also exhibited for the comparison with $-S_{cw}$. The relationships $S_{wp}\approx -S_{cp}$ and $-S_{cw}\approx S_{cc}$ can be clearly seen.

ter of mass of each polymer) in the $CaCO_3$ crystals. Such structures with $D_f\approx 2-3$ can be observed commonly for aggregation structures like silica particle aggregates,[47] silica aerogels,[51] polymer gels,[52] etc. Furthermore $D_f\approx 2.5$ can be often observed for nonequlibrium growth processes of diffusion limited aggregations or percolation clusters.[53] So our result indicates that the structure formation of $CaCO_3$ in the presence of double hydrophilic block copolymers might have similarities with these phenomena.

B. Cross terms

The cross terms $S_{ij}\,(i\neq j)$ reflect correlations between the components i and j. They are achieved together with the squared terms, S_{ii}, e.g., see Eq. (A8)

In Fig. 9 the decomposed cross terms are shown. The relationships

$$-S_{cp}\approx +S_{wp}, \quad -S_{cw}\approx S_{cc}\approx S_{ww} \tag{24}$$

are clearly found ($S_{cc}\approx S_{ww}$ is the result in Sec. IV A).

The scattering amplitude of component i at the given scattering wave number Q, $\mathbf{A}_i(Q)$, is introduced as

$$\mathbf{A}_i(Q)=\langle \exp(-i\mathbf{Q}\cdot\mathbf{r}_i)\rangle, \tag{25}$$

where the scattering length is unity (i.e., $\langle b_i\rangle=1$) and the absolute vector $\mathbf{r}_i$ points toward the arbitrary position within component i. Therefore the partial scattering function S_{ij} is described with the scattering amplitudes as

$$S_{ij}(Q)=\tfrac{1}{2}\{\mathbf{A}_i(Q)\cdot\mathbf{A}_j^*(Q)+\mathbf{A}_i^*(Q)\cdot\mathbf{A}_j(Q)\}. \tag{26}$$

The relationships of the scattering amplitudes $\mathbf{A}_i$ based on the Babinet principle (see Appendix A) are described in a complex plane as seen in Fig. 10. The example of binary systems is exhibited in Fig. 10(a), where the amplitudes are on condition of $|\mathbf{A}_1|=|\mathbf{A}_2|$ with the phase difference $\psi_{12}=\pi$ [see Eq. (A4)]. Figure 10(b) displays the situation of the amplitudes for ternary systems. Since $\mathbf{A}_1+\mathbf{A}_2+\mathbf{A}_3=0$ is met for ternary systems according to Eq. (4) or Eq. (A1), $\mathbf{A}_1$, $\mathbf{A}_2$, and $\mathbf{A}_3$ are arranged as a triangle in the complex plane. Therefore, the conditions expressed by Eq. (24) lead to the following relations in the given Q range: the scattering amplitude of water, $\mathbf{A}_w$, and the amplitude of $CaCO_3$, $\mathbf{A}_c$, are

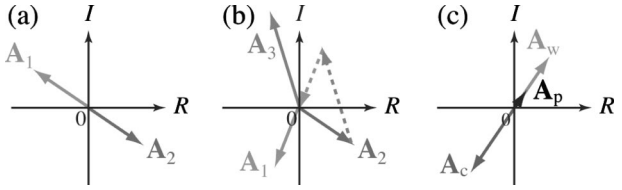

FIG. 10. Examples of the scattering amplitudes A_i on complex plane: (a) a binary system with A_1 and A_2; (b) a ternary system with A_1, A_2, and A_3; and (c) the current system with A_c, A_p, and A_w.

almost of same magnitude and nearly parallel with each other with the direction of $\mathbf{A}_c$ opposite to $\mathbf{A}_w$. Since $\mathbf{A}_p=-(\mathbf{A}_c+\mathbf{A}_w)$, $\mathbf{A}_p$ must be very small and must have the same direction as $\mathbf{A}_w$. This is depicted in Fig. 10(c), and is consistent with Eq. (24). In other words, $\mathbf{A}_p$ and $\mathbf{A}_c$ give a negative S_{cp}, which means that the polymer chains have to be distributed within the $CaCO_3$ particles. A negative S_{cp} in the Porod region ($Q>1/R_g$) can also be understood from the observation that S_{cc} is larger than $S_{ww}=S_{cc}+S_{pp}+2S_{cp}$ because of the additional surface formed by the polymers within $CaCO_3$. This observation can also be discussed in a ''thermodynamic'' picture. Since the cross terms are directly related with the second virial coefficient B_2 as $S_{ij}(Q)\propto -B_2$,[32] we have here the situation of a positive B_2, which describes an attractive interaction between the polymer and $CaCO_3$.

We can summarize that the polymers are within the $CaCO_3$ particles, and are almost homogeneously distributed. No aggregates are formed, since S_{pp} shows a plateau region in the middle of the Q range ($0.01<Q\,[\text{Å}^{-1}]<0.04$).

V. CONCLUSIONS

We have studied the effect of the double-hydrophilic block copolymer PEG-*b*-PMAA onto calcium carbonate ($CaCO_3$) morphogenesis. The polymer leads to a controlled synthesis of $CaCO_3$ with unusual morphologies. This could be demonstrated here on a more detailed basis than has been reported before in Ref. 8.

We performed small angle neutron scattering experiments applying a sophisticated contrast variation scheme, which leads to a decomposition of the obtained scattering data into the partial scattering functions of each component. This is an essential requirement for a comparison with quantitative approaches and for a detailed analysis of the role of the polymers as additives for the morphogenesis of $CaCO_3$. Furthermore, our experiments confirm the validity of a model based on the assumption of incompressibility as well as of the Babinet principle, which predicts that the scattering intensities of any ternary system can be described by the three squared-terms of the partial scattering functions.

A careful analysis of the partial scattering functions elucidated very detailed information on the structure of each component in the organic–inorganic hybrid material on the mesoscopic scale in a coherent manner. The obtained partial scattering function of polymer, S_{pp}, is roughly two orders of magnitude lower than the partial scattering function of $CaCO_3$, S_{cc}, and $S_{cc}\approx S_{ww}$ holds in the measured Q range, where S_{ww} is the partial scattering function of water. This

corresponds to a very low concentration of the polymer in the $CaCO_3$ hybrid particles, which is consistent with the results achieved by pyrolysis measurements in Appendix C 2 (5.1–5.9 wt %). At low Q, S_{pp} shows a monotonic increase obeying $I(Q) \propto Q^{-D}$ with $D=2.6$ and 2.7. This suggests that the distribution of the polymer has a mass fractal dimension. In other words, the centers of mass of the polymers are distributed in $CaCO_3$ obeying $N(r) \propto r^{-D}$ with $D=2.6-2.7$, where $N(r)$ is the number density of the polymer as a function of distance, r. Those slopes continue to $Q \approx 0.002\,\text{Å}^{-1}$, where the corresponding length scale in real space is roughly 300 nm according to the Bragg's condition of diffraction $d=2\pi/Q$, and which is the lowest limit of our experiment, so that this structure exists over a large scale (possibly up to near micron order). In the middle Q range, a plateau region is observed for S_{pp}, which is evidence that the polymer chains are isolated individually. The comparison between the partial scattering functions of water S_{ww} and $CaCO_3$ S_{cc} reveals the outer interface roughness of the $CaCO_3$ particles, which may be a trace from the aggregation of $CaCO_3$ primary particles at the early stage of the crystal formation.

The other partial scattering functions give additional significant information. Especially, the comparisons of the cross terms, S_{cp}, S_{wp}, and S_{cw}, lead to an understanding of the relationships of each scattering amplitude, and this result clearly concludes the location of the polymers, i.e., most polymers are within the $CaCO_3$ crystals.

The effect of the double hydrophilic polymer during crystallization is possibly that the polymer changes the crystallization process into an aggregation-like behavior, which may be similar to diffusion limited aggregation or percolation clusters. The significant difference from those processes is that the final $CaCO_3$ crystals have finely controlled superstructures with respect to their size and shape, like dumbbell, sphere, and others. But this point is still a mystery. Ongoing more detailed studies, e.g., about the kinetics of the crystallization process, are also essential for the comprehensive understanding.

We demonstrated in this article that our experiment applying the contrast variation neutron scattering technique is accurate enough to reveal the hidden information, even though the amount of the target material in the system is minute, and this method is almost identical to the possibility to achieve structure information with nanometer-scale resolution.

ACKNOWLEDGMENTS

This work was supported by Bundesministerium für Bildung und Forschung (BMBF) under Grant No. COE3MP and by the Max Planck Society. H.E. thanks Professor D. Richter, M. Monkenbusch, and W. Pyckhout for meaningful discussions. M. Heiderich is acknowledged for his experimental support at FZ-Jülich. Acknowledgment is also made to B. Smarsly (WAXS), I. Zenke (WAXS), C. Remde (TGA), and R. Pitschke (SEM) for the characterization of $CaCO_3$ at MPI-Golm. Th. Goldschmidt AG (Essen, Germany) is acknowledged for providing the block copolymer sample.

APPENDIX A: THE MULTICOMPONENT BABINET PRINCIPLE

The Babinet principle can be derived from geometric justification.[54] Let us assume a multicomponent system with p different species as in Sec. II A, however, here we assume the scattering contrasts of all components are the same. In this case, there is no scattering arising, which has a relationship as follows:

$$\sum_{i=1}^{p} A_i(Q) = 0, \tag{A1}$$

where $A_i(Q)$ is a scattering amplitude of species i with the unit scattering length defined in Eq. (25). This relationship is called "the Babinet principle," and $A_k(Q)$ reflects simply the geometry of component k.

Equation (A1) can be easily understood if we consider a binary system. In that case, the total scattering intensity from species 1 and species 2 is given by

$$\frac{d\Sigma}{d\Omega}(Q) = \rho_1^2 S_{11}(Q) + 2\rho_1\rho_2 S_{12}(Q) + \rho_2^2 S_{22}(Q), \tag{A2}$$

which is derived from Eq. (1). Here, for any binary system, the scattering from species 1 and species 2 should be the same, i.e.,

$$S_{11}(Q) = S_{22}(Q) = -S_{12}(Q). \tag{A3}$$

Equation (A3) means that the amplitudes of $A_1(Q)$ and $A_2(Q)$ are the same, therefore the difference of the phase between $A_1(Q)$ and $A_2(Q)$ is just π. Finally we can derive

$$A_1(Q) = -A_2(Q) \Leftrightarrow A_1(Q) + A_2(Q) = 0. \tag{A4}$$

This discussion can easily be applied to multicomponent systems and we achieve Eq. (A1), which leads to

$$A_k(Q) = -\sum_{i \neq k}^{p} A_i(Q). \tag{A5}$$

Therefore the corresponding partial scattering function $S_{kk}(Q)$ is given by

$$\begin{aligned} S_{kk}(Q) &= A_k(Q)A_k^*(Q) \\ &= \sum_{i \neq k}^{p} A_i(Q)A_i^*(Q) + \sum_{i,j \neq k; i<j}^{p} \{A_i(Q) \\ &\quad \times A_j^*(Q) + A_i^*(Q)A_j(Q)\} \\ &= \sum_{i \neq k}^{p} S_{ii}(Q) + 2\sum_{i,j \neq k; i<j}^{p} S_{ij}(Q). \end{aligned} \tag{A6}$$

Equation (A6) is the same as Eq. (7).

Equations (7) and (A6) allow one to eliminate one species, e.g., eliminating the species represented by index k, we can derive

$$\frac{d\Sigma}{d\Omega}(Q)=\sum_{i\neq k}^{p}(\rho_i-\rho_k)^2 S_{ii}(Q)$$

$$+2\sum_{i,j\neq k;i<j}^{p}(\rho_i-\rho_k)(\rho_j-\rho_k)S_{ij}(Q). \quad \text{(A7)}$$

Equation (A7) is known as the general description of elastic scattering with partial scattering functions in the basis of incompressibility or the Babinet principle.[32,55]

We can also substitute all the squared terms $S_{kk}(Q)$ with the cross terms $S_{ij}(Q)\,(i\neq j)$ by Eq. (6). Then we achieve

$$\frac{d\Sigma}{d\Omega}(Q)=-\sum_{i\neq j;i<j}^{p}(\rho_i-\rho_j)^2 S_{ij}(Q). \quad \text{(A8)}$$

Equation (A8) is equivalent to Eq. (A7). Both Eqs. (A7) and (A8) indicate that the number of partial scattering functions for the description of the scattering intensity is at least ${}_pC_2 = p!/\{(p-2)!\cdot 2\}$ based on the assumption of incompressibility.

APPENDIX B: DECOMPOSITION FROM PARTIAL SCATTERING FUNCTIONS TO SCATTERING LENGTH DENSITIES

If we know the partial scattering functions, we can decompose the intensity into scattering length densities, i.e., for ternary systems,

$$\underline{S}\cdot\begin{pmatrix}\Delta\rho_{11}^2\\ \Delta\rho_{12}^2\\ \Delta\rho_{22}^2\end{pmatrix}=\begin{pmatrix}\frac{d\Sigma}{d\Omega}(Q_1)\\ \vdots\\ \frac{d\Sigma}{d\Omega}(Q_n)\end{pmatrix}, \quad \text{(B1)}$$

where

$$\underline{S}=\begin{pmatrix}S_{11}(Q_1) & S_{12}(Q_1) & S_{22}(Q_1)\\ \vdots & \vdots & \vdots\\ S_{11}(Q_n) & S_{12}(Q_n) & S_{22}(Q_n)\end{pmatrix} \quad \text{(B2)}$$

and

$$\Delta\rho_{11}^2=(\rho_1-\rho_3)^2,$$

$$\Delta\rho_{12}^2=2(\rho_1-\rho_3)(\rho_2-\rho_3), \quad \text{(B3)}$$

$$\Delta\rho_{22}^2=(\rho_2-\rho_3)^2.$$

Equation (B3) is based on Eq. (A7). In Eq. (B1), both $S_{ij}(Q_n)$ and $(d\Sigma/d\Omega)(Q_n)$ for the whole experimental Q range of the single scattering result are included into the matrix $\underline{S}$ in order to decompose each $\Delta\rho_{ij}^2$ with solving $\underline{S}^T$.

TABLE IV. Extracted parameters from $S_{pp}(Q)$.

[Polymer]/[$CaCO_3$]	D_f	ξ (μm)	$\mathcal{R}_g$ (Å)
0.3	2.68±0.02	0.29±0.17	35±1
0.9	2.61±0.04	0.10±0.02	32±2

TABLE V. Calculated scattering length densities of water ρ_w and estimated values $\acute{\rho}_w$ for the contrast variation experiments. The "Error" is the averaged difference (percentage) between an experimental value and a reconstructed value.

	[Polymer]/[$CaCO_3$]=0.3		[Polymer]/[$CaCO_3$]=0.9	
Increment	ρ_w	$\acute{\rho}_w$	ρ_w	$\acute{\rho}_w$
1	4.895	4.998	4.895	4.998
2	4.784	4.880	4.811	4.893
3	4.727	4.670	4.730	4.821
4	4.643	4.628	4.642	4.618
5	4.489	4.539	4.476	4.486
D_2O	6.355	6.292	6.355	6.292
Error	2.364	0.926	2.218	1.796

The obtained $\Delta\rho_{ij}^2$ may lead to optimized partial scattering functions. The experimental intensities are compared with reconstruction intensities, which are reconstructed with the estimated scattering length densities and the obtained partial scattering functions [i.e., calculating the right-hand side of Eq. (10)]. This method can be used to check the quality of the initial estimation of the scattering length densities of each component.

The iterative procedure is as follows: First of all, the errors between the experimental values and the reconstructed values are summed up, where the reconstruction is done by the inferred partial scattering functions and the estimated scattering length densities with Eq. (10). Second, the $\Delta\rho_{ij}^2$ are estimated by Eq. (B1), i.e., the inferred partial scattering functions lead to the optimized scattering length densities for each scattering intensity. These scattering length densities are used to decompose the experimental intensities into the partial scattering functions again. Finally, the total sum of errors is calculated with these "renewed" partial scattering functions, and compared with the former values. When the updated error is bigger than the former one, the procedure was stopped, otherwise it is repeated until the error reaches the minimum.

We mention that this iterative method requires certain realistic constraints, since without these constraints the values easily lead to unrealistic results. In our case, the scattering length densities of $CaCO_3$ and the polymer were fixed, and only the scattering length densities of the solvent (water)

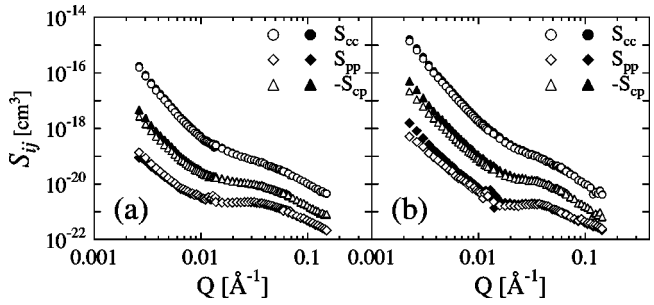

FIG. 11. Decomposed partial scattering functions: S_{cc}(●), S_{pp}(◆), and S_{cp}(▲), respectively, for (a) sample [polymer]/[$CaCO_3$]=0.3 and (b) sample [polymer]/[$CaCO_3$]=0.9. Open-markers are based on the initial scattering length densities and closed markers are the results from the corrected values.

was allowed to move as a parameter. Additionally, the scattering length densities of the solvent for the increment-1 and D_2O were forced to be identical for sample [polymer]/[$CaCO_3$]=0.3 and 0.9, since we used the same solvents for these experiments.

The initial estimation of the scattering length densities and the obtained values with this procedure are listed in Table V. About 2% collection is the maximum, and this reflects the accuracy of these experimental procedures and this error probably originates from inaccuracies[56] during mixing H_2O and D_2O. In Fig. 11 the resulting partial scattering functions $S_{cc}(Q)$, $S_{pp}(Q)$, and $S_{cp}(Q)$ are displayed. The obtained cross term $S_{cp}(Q)$ is negative for the whole measured Q range, so that $-S_{cp}(Q)$ is shown in a double-logarithmic scale. The effects of scattering length density corrections are shown as open markers and closed markers in Fig. 11. The corrected scattering length densities mainly affect S_{pp} and S_{cp}, as shown in Fig. 11, especially at low Q, but these are only minor effects, which do not change the analytic results dramatically. This procedure checked the quality of the estimation of the scattering length densities.

APPENDIX C: CHARACTERIZATION OF $CaCO_3$ PARTICLES

1. Scanning electron microscopy

The obtained crystals were checked by scanning electron microscopy (SEM) on a Carl Zeiss DSM 940A (Jena, Germany) to confirm the obtained morphology.

Figure 1 depicts the observed electron microscopy pictures of the materials. The effect of the polymer is clearly shown, that is, without polymer only the well-established rhombohedral crystals (calcite) were obtained, on the other hand, mainly dumbbell structures were obtained with polymer. Moreover the sizes of crystals are strongly affected by the mass ratio [polymer]/[$CaCO_3$]. It is evident that the crystal size with [polymer]/[$CaCO_3$]=0.3 is bigger than that of [polymer]/[$CaCO_3$]=0.9. Since all the crystals were prepared under vigorous stirring during the whole crystallization process, the obtained morphologies were dumbbell-shaped for both of the samples with polymer, which is different from the results in Ref. 8 where the crystals were grown on standing for 24 h after 1 min stirring at the mixing of chemicals.

TABLE VI. Volume fractions of polymer ϕ_p in $CaCO_3$ determined by thermogravimetry analysis, and crystallite sizes L determined by WAXS (the resolution of the spectrometer is taken into account).

Sample	[Polymer]/[$CaCO_3$]	ϕ_p (vol %)	L (Å)
1	0	0	540±115
2	0.3	0.127	230±26
3	0.9	0.145	215±18

2. Thermogravimetry analysis

Thermogravimetry analysis was performed to investigate the mass fraction of the polymer in the crystals with a Netzsch TG209 (Selb, Germany).

The samples were heated up to about 900 °C gradually for 45 min under nitrogen atmosphere, and the mass reduction was measured against temperature.

Figure 12 gives the results obtained from $CaCO_3$ crystals with different polymer concentrations. We assume that the reduction of polymer mass is represented between 150 and 600 °C, since the polymer contains water which first evaporates (about 2 wt %). We can see the quick decrease of the total mass over 600 °C, which corresponds to the thermal decomposition of $CaCO_3$ to CaO. The achieved mass ratios of the polymer are 5.1 wt % for the crystal prepared with [polymer]/[$CaCO_3$]=0.3, and 5.9 wt % for [polymer]/[$CaCO_3$]=0.9, which correspond to 12.7 vol % ([polymer]/[$CaCO_3$]=0.3) and 14.5 vol % ([polymer]/[$CaCO_3$]=0.9), respectively. These results imply that the most of the polymers were not included into $CaCO_3$ particles. All the obtained values and the other parameters are summed up in Table VI.

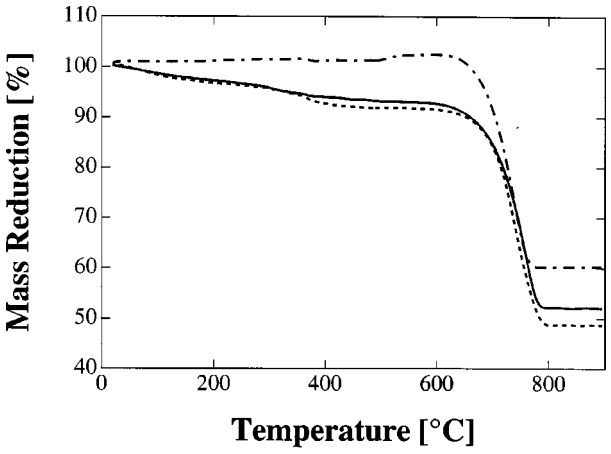

FIG. 12. Thermogravimetry measurement profiles for $CaCO_3$ without polymer (-·-), with polymer concentration [polymer]/[$CaCO_3$]=0.3 (—), and with polymer [polymer]/[$CaCO_3$]=0.9 (---), respectively.

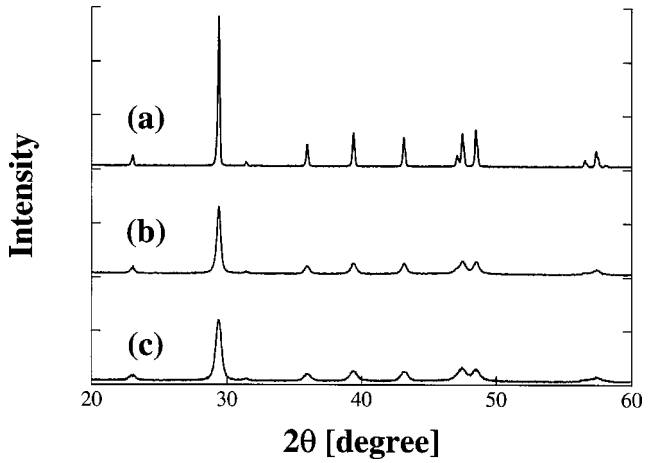

FIG. 13. Wide angle x-ray scattering profiles for (a) $CaCO_3$ without polymer, (b) with polymer [polymer]/[$CaCO_3$]=0.3, and (c) [polymer]/[$CaCO_3$]=0.9.

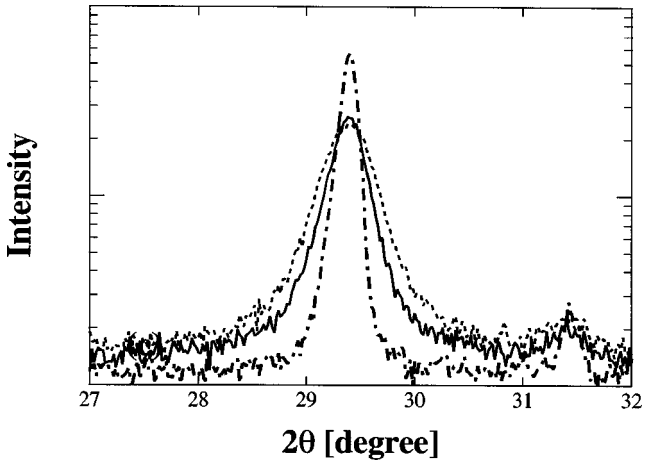

FIG. 14. Wide angle x-ray scattering profiles around [104] peaks for $CaCO_3$ without polymer (-··-), with polymer [polymer]/[$CaCO_3$]=0.3 (—), and [polymer]/[$CaCO_3$]=0.9 (---).

3. Wide angle x-ray scattering

Wide angle x-ray scattering (WAXS) measurements were used for the determination of the structures of the crystals by a PDS120 diffractometer (Nonius GmbH, Solingen) with Cu K_α radiation. It is well known that there are three anhydrous mineral forms of $CaCO_3$, which are calcite (trigonal), vaterite (hexagonal), and aragonite (orthorhombic). They have different crystal structures and symmetries, where calcite is the most stable of them in most environments[37] especially at the applied conditions. As showing in Fig. 13, the obtained x-ray diffraction patterns exhibit only sharp calcite reflections, where the peak positions are not affected by the addition of polymer. This confirms that the crystal superstructures are composed of well-crystallized calcite crystals.

On the other hand, Fig. 14 shows the [104] peaks which get broader with increasing the concentration of polymer. The peak width can be related to the crystallite defect size L by the well-known Scherrer formula[57] as

$$L=\frac{K\lambda}{\beta_m \cos(\theta)}, \tag{C1}$$

where λ is the x-ray wavelength, θ is the diffraction angle, and β_m is the linewidth of the diffraction profile. The constant K depends on the morphology of the crystallite and may be unity in the case that L is the thickness of the crystal. In Table VI, the obtained primary crystallite defect sizes L are displayed. It is cleary visible that the addition of polymer leads to an efficient decrease of the crystallite size. The size L is originated from the orientation of the crystallite, which is insensitive for small angle scattering (we discussed in Sec. IV A). But this broadening of the scattering peak is also a clear effect of the polymer addition.

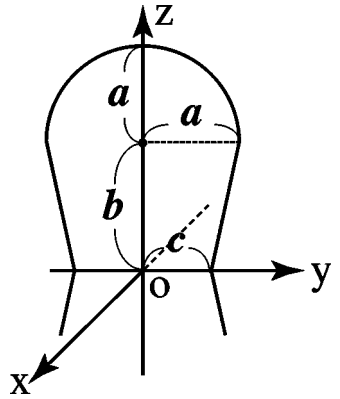

FIG. 15. Diagram of a model for a dumbbell form consisting of hemispheres with radius a and frustums with height b and top face and base radii a and c where the z axis is the rotating axis, i.e., the body has a rotational symmetry around the z axis as well as $x-y$ plane symmetry.

APPENDIX D: RADIUS OF GYRATION

To compare the obtained radii of gyration of $CaCO_3$ particles in Sec. IV from the partial scattering function of $CaCO_3$, S_{cc}, with the observed SEM pictures (Fig. 1), the radius of gyration for a dumbbell form and a rhombohedron is calculated.

1. Dumbbell form

We model a dumbbell form as described in Fig. 15, where the body is characterized by three lengths a, b, and c. A radius of gyration R_g is defined as

$$\overline{R_g^2}=\frac{1}{z}\sum_{i=1}^{z} r_i^2, \tag{D1}$$

where the body is made of z identical elements and r_i is a distance between the ith element and the center of mass. Therefore, taking into account the symmetry of the modeled dumbbell form, which has a z-axis cylindrical symmetry and $x-y$ plane symmetry, the R_g can be calculated in integral form as follows:

$$\overline{R_g^2}=\frac{\{\int_0^{2\pi}d\theta\int_0^b dz\int_0^{c+(a-c)/bz}dr+\int_0^{2\pi}d\theta\int_b^{a+b}dz\int_0^{\sqrt{a^2-(z-b)^2}}dr\}r(r^2+z^2)}{\{\int_0^{2\pi}d\theta\int_0^b dz\int_0^{c+(a-c)/bz}dr+\int_0^{2\pi}d\theta\int_b^{a+b}dz\int_0^{\sqrt{a^2-(z-b)^2}}dr\}r}$$
$$=(12a^5+18a^4b+20a^3b^2+6a^2b^3+3a^3bc3ab^3c+3a^2bc^2+b^3c^23abc^3+3bc^4)/\{10(2a^3+a^2b+abc+bc^2)\}. \tag{D2}$$

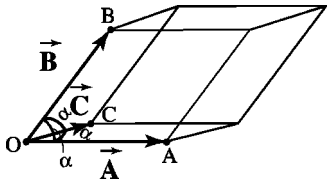

FIG. 16. A rhombohedron where $|\vec{A}|=|\vec{B}|=|\vec{C}|=L$ and $\angle AOB=\angle BOC=\angle COA=\alpha$.

2. Rhombohedral form

A rhombohedron is a six-sided prism whose sides are parallelograms with same lengths.[58] Therefore a rhombohedron is characterized by

$$|\vec{A}|=|\vec{B}|=|\vec{C}|=L \tag{D3}$$

and

$$\vec{A}\cdot\vec{B}=\vec{B}\cdot\vec{C}=\vec{C}\cdot\vec{A}=L^2\cos\alpha, \tag{D4}$$

where $\vec{A}$, $\vec{B}$, and $\vec{C}$ are linearly independent which three sides of a rhombohedron (see Fig. 16), and α is an interior angle of two of these vectors with $2\pi/3>\alpha\neq\pi/2$.

Next, the unit vectors which are parallel to $\vec{A}$, $\vec{B}$, and $\vec{C}$ are defined as

$$\vec{a}=\frac{\vec{A}}{|\vec{A}|},\quad \vec{b}=\frac{\vec{B}}{|\vec{B}|},\quad \vec{c}=\frac{\vec{C}}{|\vec{C}|}. \tag{D5}$$

With $\vec{a}$, $\vec{b}$, and $\vec{c}$, the position vector in a rhombohedral $\vec{r}_G$, whose origin is the center of mass of the rhombohedral, can be given by

$$\vec{r}_G=A\vec{a}+B\vec{b}+C\vec{c};\quad \left(-\frac{L}{2}\leqslant A,B,C\leqslant\frac{L}{2}\right), \tag{D6}$$

so that

$$|\vec{r}_G|^2=A^2+B^2+C^2+2(AB+BC+CA)\cos\alpha. \tag{D7}$$

And the volume of a rhombohedron can be expressed by

$$V=|\vec{A}||\vec{B}||\vec{C}|\cdot[(\vec{a}\times\vec{b})\cdot\vec{c}] \tag{D8}$$

with $\vec{a}$, $\vec{b}$, and $\vec{c}$. Equation (D8) simply leads to

$$V=L^3\sin\alpha\cdot\sqrt{\frac{1+\cos\alpha-2\cos^2\alpha}{1+\cos\alpha}}. \tag{D9}$$

Therefore, taking acount of symmetry, the radius of gyration of a rhombohedron can be calculated as

$$\overline{R_g^2}=\frac{\int_0^{L/2}dA\int_0^{L/2}dB\int_0^{L/2}dC\{A^2+B^2+C^2+2(AB+BC+CA)\cos\alpha\}V(\alpha)}{\int_0^{L/2}dA\int_0^{L/2}dB\int_0^{L/2}dCV(\alpha)}$$
$$=\left(\frac{1}{4}+\frac{3}{8}\cos\alpha\right)L^2, \tag{D10}$$

where

$$V(\alpha)=\sin\alpha\cdot\sqrt{\frac{1+\cos\alpha-2\cos^2\alpha}{1+\cos\alpha}}, \tag{D11}$$

which is from Eq. (D9).

[1] S. Mann, J. Webb, and R. J. P. Williams, *Biomineralization, Chemical and Biochemical Perspectives* (VCH, Weinheim, 1989).
[2] S. Mann, *Biomimetic Materials Chemistry* (VCH, Weinheim, 1995).
[3] H. Cölfen, Macromol. Rapid Commun. **22**, 219 (2001).
[4] L. Qi, H. Cölfen, and M. Antonietti, Angew. Chem., Int. Ed. Engl. **39**, 604 (2000).
[5] K. L. Robinson, J. V. M. Weaver, S. P. Armes, E. D. Marti, and F. C. Meldrum, J. Mater. Chem. **12**, 890 (2002).
[6] M. Antonietti, M. Breulmann, C. G. Göltner, H. Cölfen, K. K. W. Wong, D. Walsh, and S. Mann, Chem.-Eur. J. **4**, 2493 (1998).
[7] J. M. Marentette, J. Norwig, E. Stoekelmann, W. H. Meyer, and G. Wegner, Adv. Mater. (Weinheim, Ger.) **9**, 647 (1997).
[8] H. Cölfen and L. Qi, Chem.-Eur. J. **7**, 106 (2001).
[9] S.-H. Yu, H. Cölfen, and M. Antonietti, J. Phys. Chem. B **107**, 7396 (2003).
[10] M. Oner, W. H. Meyer, and G. Wegner, Chem. Mater. **10**, 406 (1998); A. Taubert, G. Glasser, and D. Palms, Langmuir **18**, 4488 (2002).
[11] F. Bouyer, C. Gérardin, F. Fajula, J.-L. Putaux, and T. Chopin, Colloids Surf., A **217**, 179 (2003); C. Gérardin, N. Sanson, F. Bouyer, F. Fajula, J.-L. Putaux, and T. Chopin, Angew. Chem., Int. Ed. Engl. **42**, 3681 (2003).
[12] S.-H. Yu, M. Antonietti, H. Clfen, and M. Giersig, Angew. Chem., Int. Ed. Engl. **41**, 2356 (2002).
[13] L. Qi, H. Cölfen, and M. Antonietti, Nano Lett. **1**, 61 (2001).
[14] D. Zhang, L. Qi, J. Ma, and H. Cheng, Chem. Mater. **13**, 2753 (2001).
[15] L. H. Bronstein, S. N. Sidorov, P. M. Valetsky, J. Hartmann, H. Cölfen, and M. Antonietti, Langmuir **15**, 6256 (1999).
[16] Y. Mastai, M. Sedlák, H. Cölfen, and M. Antonietti, Chem.-Eur. J. **8**, 2429 (2002).
[17] Y. Mastai, J. Rudloff, H. Cölfen, and M. Antonietti, Chem Phys Chem. **3**, 119 (2002).
[18] J. Rudloff and H. Cölfen, Langmuir **20**, 991 (2004).
[19] R. Kniep and S. Busch, Angew. Chem. **108**, 2787 (1996); Angew. Chem., Int. Ed. Engl. **35**, 2624 (1996).
[20] S. Busch, H. Dolhaine, A. DuChesne, S. Heinz, O. Hochrein, F. Laeri, O. Podebrad, U. Vietze, T. Weiland, and R. Kniep, Eur. J. Inorg. Chem. **1999**, 164.
[21] G. E. Bacon, *Neutron Diffraction* (Clarendon, Oxford, 1975).
[22] M. H. G. Duits, R. P. May, A. Vrij, and C. G. de Kruif, J. Chem. Phys. **94**, 4521 (1991).
[23] P. Bartlett and R. H. Ottewill, J. Chem. Phys. **96**, 3306 (1992).
[24] D. Richter, D. Schneiders, M. Monkenbusch, L. Willner, L. J. Fetters, J. S. Huang, and M. Lin, Macromolecules **30**, 1053 (1997).
[25] A. Poppe, L. Willner, J. Allgaier, J. Stellbrink, and D. Richter, Macromolecules **30**, 7462 (1997).
[26] H. Endo, J. Allgaier, G. Gompper, B. Jakobs, M. Monkenbusch, D. Richter, T. Sottmann, and R. Strey, Phys. Rev. Lett. **85**, 102 (2000).
[27] J. S. Pedersen and L. Arleth, Phys. Rev. E **63**, 061406 (2001).

[28] R. Willumeit, N. Burkhardt, G. Diedrich, J. Zhao, K. H. Nierhaus, and H. B. Stuhrmann, J. Mol. Struct. **383**, 201 (1996).
[29] N. Niimura, Y. Minezaki, I. Tanaka, S. Fujiwara, and M. Ataka, J. Cryst. Growth **200**, 265 (1999).
[30] H. Endo, M. Mihailescu, M. Monkenbusch, J. Allgaier, G. Gompper, D. Richter, B. Jakobs, T. Sottmann, R. Strey, and I. Grillo, J. Chem. Phys. **115**, 580 (2001).
[31] H. Endo, D. Schwahn, and H. Cölfen, J. Appl. Crystallogr. **36**, 568 (2003).
[32] J. S. Higgins and H. C. Benoit, *Polymers and Neutron Scattering* (Clarendon, Oxford, 1994).
[33] A. Botti, W. Pyckhout-Hintzen, D. Richter, V. Urban, E. Straube, and J. Kohlbrecher, Polymer **44**, 7505 (2003).
[34] A set of equations that is *degenerate* is called *singular. Singular value decomposition* (SVD) is a technique for dealing with sets of equations or matrices which are either *singular* or else numerically very close to *singular*. SVD is a standard subroutine included in the commercial subroutine packages, like *IMSL* or *NAG* libraries, see their WWW-Servers of *Visual Numerics, Inc.*: http://www.vni.com or *Numerical Algorithms Group, Ltd.*: http://www.nag.com. In this study, the *SVD* in *IMSL subroutine library* is used. A more detailed description of SVD can be found in W. H. Press *et al.*, *Numerical Recipes* (Cambridge University Press, Cambridge, 1986).
[35] Instrumental details of *KWS*−1 are given on the web site: ''http://www.fz-juelich.de/iff/wns_kws1''.
[36] K. Schilling, Dissertation, University of Potsdam, 1999.
[37] See, e.g., *Gmelin Handbook of Inorganic Chemistry* (Springer, Berlin, 1986).
[38] G. Porod, in *Small Angle X-ray Scattering*, edited by O. Glatter and O. Kratky (Academic, New York, 1982).
[39] The Gaussian roughness of the interface σ originates from the hypothesis that the scattering length density profile changes smoothly across the interface, which may be approximated by an error-function shape.
[40] L. Auvray and P. Auroy, in *Neutron, X-ray and Light Scattering: Introduction to an Investigative Tool for Colloidal and Polymeric Systems*, edited by P. Lindner and Th. Zemb (North-Holland, Amsterdam, 1991).
[41] R. Kirste and G. Porod, Koll. Z., Z. für Polym. **184**, 1 (1969).
[42] A Gaussian ellipsoid was assumed as the resolution function in this study according to J. S. Pedersen, D. Posselt, and K. Mortensen, J. Appl. Crystallogr. **23**, 321 (1990).
[43] G. Beaucage, J. Appl. Crystallogr. **28**, 717 (1995).
[44] We mention that the used resolution function and Eq. (18) are approximate, so that the obtained R_g may contain the error originating from those uncertainties.
[45] Four different symbols for the radius of gyration are used in this literature, i.e., R_g, r_g, $\mathcal{R}_g$, and $\mathbb{R}_g$; which are to clarify their different origins. R_g is obtained from the total size of $CaCO_3$ crystals; on the other hand, r_g can be related to the interfacial structure of $CaCO_3$ crystals. $\mathcal{R}_g$ is the radius of gyration of the single polymer chain [see Eq. (21)], and $\mathbb{R}_g$ is related to the size of the polymer aggregates [see Eq. (23)].
[46] S. K. Sinha, T. Freltoft, and J. Kjems, in *Kinetics of Aggregation and Gelation*, edited by F. Family and D. P. Landau (Elsevier, Amsterdam, 1984), p. 87.
[47] T. Freltoft, J. Kjems, and S. K. Sinha, Phys. Rev. B **33**, 269 (1986).
[48] G. Beaucage, J. Appl. Crystallogr. **29**, 134 (1996).
[49] S. Kawaguchi, G. Imai, J. Suzuki, A. Miyahnara, T. Kitano, and K. Ito, Polymer **38**, 2885 (1995).
[50] S. K. Sinha, Physica D **38**, 310 (1989).
[51] R. Vacher, T. Woignier, J. Pelous, and E. Courtens, Phys. Rev. B **37**, 6500 (1988).
[52] J. E. Martin and J. P. Wilcoxon, Phys. Rev. A **39**, 252 (1989).
[53] D. W. Schaefer, J. E. Martin, and K. D. Keefer, in *Physics of Finely Divided Matter*, edited by N. Bocarra and M. Daoud (Springer, Berlin, 1985).
[54] M. Born and E. Wolf, *Principles of Optics*, 7th ed. (Cambridge University Press, Cambridge, 1999).
[55] H. Benoit, J. Koberstein, and L. Leibler, Makromol. Chem. Suppl. **4**, 85 (1981).
[56] Since the additions of H_2O were done on the milligram scale for each step, the error may be unignorable even with checking by a chemical balance.
[57] A. Guinier, *X-ray Diffraction in Crystals, Imperfect Crystals, and Amorphous Bodies* (Dover, New York, 1994).
[58] See, e.g., A. Putnis, *Introduction to Mineral Science* (Cambridge University Press, Cambridge, 1992).